

RESEARCH ARTICLE

Open Access



Cryptomelane formation from nanocrystalline vernadite precursor: a high energy X-ray scattering and transmission electron microscopy perspective on reaction mechanisms

Sylvain Grangeon^{1*}, Alejandro Fernandez-Martinez^{2,3}, Fabienne Warmont⁴, Alexandre Gloter⁵, Nicolas Marty¹, Agnieszka Poulain⁶ and Bruno Lanson^{2,3}

Abstract

Background: Vernadite is a nanocrystalline and turbostratic phyllomanganate which is ubiquitous in the environment. Its layers are built of $(\text{MnO}_6)^{8-}$ octahedra connected through their edges and frequently contain vacancies and (or) isomorphic substitutions. Both create a layer charge deficit that can exceed 1 valence unit per layer octahedron and thus induces a strong chemical reactivity. In addition, vernadite has a high affinity for many trace elements (e.g., Co, Ni, and Zn) and possesses a redox potential that allows for the oxidation of redox-sensitive elements (e.g., As, Cr, Tl). As a result, vernadite acts as a sink for many trace metal elements. In the environment, vernadite is often found associated with tectomanganates (e.g., todorokite and cryptomelane) of which it is thought to be the precursor. The transformation mechanism is not yet fully understood however and the fate of metals initially contained in vernadite structure during this transformation is still debated. In the present work, the transformation of synthetic vernadite ($\delta\text{-MnO}_2$) to synthetic cryptomelane under conditions analogous to those prevailing in soils (dry state, room temperature and ambient pressure, in the dark) and over a time scale of ~ 10 years was monitored using high-energy X-ray scattering (with both Bragg-rod and pair distribution function formalisms) and transmission electron microscopy.

Results: Migration of Mn^{3+} from layer to interlayer to release strains and their subsequent sorption above newly formed vacancy in a triple-corner sharing configuration initiate the reaction. Reaction proceeds with preferential growth to form needle-like crystals that subsequently aggregate. Finally, the resulting lath-shaped crystals stack, with $n \times 120^\circ$ ($n = 1$ or 2) rotations between crystals. Resulting cryptomelane crystal sizes are $\sim 50\text{--}150$ nm in the **ab** plane and $\sim 10\text{--}50$ nm along **c***, that is a tenfold increase compared to fresh samples.

Conclusion: The presently observed transformation mechanism is analogous to that observed in other studies that used higher temperatures and (or) pressure, and resulting tectomanganate crystals have a number of morphological characteristics similar to natural ones. This pleads for the relevance of the proposed mechanism to environmental conditions.

Keywords: Vernadite, $\delta\text{-MnO}_2$, Cryptomelane, Phyllomanganate, Tectomanganate, Pair Distribution Function, Bragg rod, High-energy X-ray scattering, X-ray diffraction, Transmission electron microscopy

*Correspondence: s.grangeon@brgm.fr

¹ BRGM, 3 Avenue Guillemin, 45060 Orléans Cedex 2, France

Full list of author information is available at the end of the article

Background

Vernadite (and δ -MnO₂, its synthetic analogue) is a nanocrystalline turbostratic birnessite, a phylломanganate whose layers are built of (MnO₆)⁸⁻ octahedra connected through their edges and separated by hydrated interlayer cations. Vernadite is ubiquitous in the environment, and probably results mainly from the aqueous oxidation of Mn²⁺ by bacteria [1–3], fungi [4–6], and higher living forms [7], as abiotic oxidation catalyzed by mineral surfaces is about two orders of magnitude slower [8–11]. Vernadite layers frequently contain vacancies and (or) isomorphic substitutions (substitution of layer Mn⁴⁺ by a foreign cation, e.g., Co³⁺, Mn³⁺, or Ni²⁺ [12–14]), both types of defects inducing a layer charge deficit. For example, layer charge was 0.86–1.22 and 1.58 valence unit (v.u.) per layer octahedron for samples produced by fungal strains [4] and by grass roots [7], respectively. Layer charge induces a high chemical reactivity, which is reinforced by the nanometric size of vernadite (typically 5–50 nm in the layer plane—[1, 15, 16]) and the induced proportion of reactive edge sites [3, 17, 18]. Vernadite also presents a high affinity for many trace elements such as transition metals (e.g., Co, Ni, Zn), actinides and rare earth elements [14, 19–36]. For example, vernadite is the main sink for Ni in mixed mineral/biotic systems (vernadite and *Pseudomonas Putida* biofilm [37, 38]). Vernadite can also oxidize organic pollutants and redox-sensitive elements such as arsenic [39–42], chromium [39–43], and thallium [34, 44], possibly because of the common coexistence of heterovalent Mn cations in its structure. Specifically, Mn³⁺ cations can be present both within octahedral layers and (or) adsorbed above layer vacancies, forming triple-corner-sharing complexes (^{TC}Mn³⁺; Fig. 1 in [45]).

Additional interest in understanding vernadite structure arises from its frequent association with tectomanganates (i.e., tunnel structures) in the environment. Tectomanganates include a variety of minerals with [*n* × *m*] tunnel sizes, where *n* stands for the number of octahedra connected to form the “walls” of the tunnels, whereas *m* stands for the number of octahedra forming the “ceiling” and the “floor”. For example, vernadite is frequently found with todorokite and cryptomelane, [3 × 3] and [2 × 2] tunnel structures, respectively [26, 46–48]. Tectomanganates can form from phylломanganate precursors [46, 49, 50] provided that they possess a particular crystal-chemistry, for example possess Mn³⁺ [51, 52]. Phylломanganate-to-tectomanganate reaction mechanisms have been widely investigated owing to the tectomanganate potential as octahedral molecular sieves. Reaction products must have homogenous tunnel size for this purpose to achieve optimal efficiency and the relation between the layered precursor and the resulting

tunnel structure is studied with special care (e.g., [49] and references therein and [53, 54]). Relations between layer and tunnel structures is also of interest in natural settings, mainly because defective todorokite (i.e., having mainly [3 × 3] tunnel size, together with [3 × *m*] size, *m* varying from 2 to 5) is found associated with vernadite in oceanic ferromanganese nodules. These nodules consist of alternating layers of iron and manganese oxides [31, 34, 55], the latter containing typically over 1 wt% of Ni [56–58], and are increasingly considered for their potential as a source of strategic trace metals including rare-earth elements. A comprehensive understanding of phylломanganate to tectomanganate transformation, at the atomic scale, thus appears key to an improved prediction and modeling of the impact of structure defects (layer vacancies and isomorphic substitutions) on the fate of trace elements.

Observations of vernadite-to-todorokite transformation in natural samples are scarce, but suggest a topotactic reaction [46]. It was first reported by Golden and coworkers [59] for synthetic analogues and has since been repeatedly described for a variety of hydrothermal protocols. Recently, these protocols were reviewed by Atkins and coworkers [60], who also characterized the structural mechanisms of the δ -MnO₂ to todorokite transformation at 100 °C and atmospheric pressure. These authors described the transformation as a four-stage process, starting with the formation of todorokite tunnel walls via layer kinking, followed by the growth of the particles along the [010] direction (i.e., along the tunnel direction) during a dissolution–recrystallization step and subsequent oriented attachment of the resulting particles along the [100] direction to form todorokite laths which then stack. A last step is described as the growth of todorokite crystals by Ostwald ripening. These authors mentioned also that the density of structural Mn³⁺ has to be “significant” to allow for a complete transformation and linked this condition to the ability of Mn³⁺ to induce layer kinking, owing to its Jahn–Teller distorted environment. Another important parameter appears to be the presence of an interlayer cation enforcing a ~10 Å layer-to-layer distance (e.g., Mg²⁺).

Similar to todorokite, cryptomelane formation in environmental conditions is little documented. A recent study [49] focused on δ -MnO₂ samples equilibrated at pH values ranging from 3 to 10. Initially, all samples had a similar number of layer Mn³⁺ per octahedron (0.10 ± 0.02–0.14 ± 0.02), whereas the number of interlayer ^{TC}Mn³⁺ increased with decreasing equilibration pH. Although such evolution might seem counter-intuitive because, by analogy with clay minerals, decreasing pH should increase proton competition for sorption [61–63], it is made possible by the fact that pH decrease is accompanied by partial layer dissolution and thus

by an increase of Mn concentration in the equilibrium solution, making it possible for dissolved Mn to adsorb above vacancies [64]. Structural formulae from samples initially equilibrated at pH 3 and 10 were $\text{Na}_{0.06}^+(\text{H}_2\text{O})_{0.30}\text{Mn}_{0.185}^{3+}[\text{Mn}_{0.12}^{3+}\text{Mn}_{0.71}^{4+}\text{Vac}_{0.17}\text{O}_2]$ and $\text{Na}_{0.27}^+(\text{H}_2\text{O})_{0.30}\text{Mn}_{0.095}^{3+}[\text{Mn}_{0.10}^{3+}\text{Mn}_{0.76}^{4+}\text{Vac}_{0.14}\text{O}_2]$, respectively. In these formulae, species within brackets form the layer, those to the left the interlayer, Vac stands for layer vacancies, and all interlayer Mn sites (TC and triple-edge sharing [45] configurations) are summed. Samples were then dried, and aged in the dark. With time, it was observed that layer Mn^{3+} leaves the layer to form $^{\text{TC}}\text{Mn}^{3+}$ above the newly generated vacancy. Partial transformation to cryptomelane was observed only for pH 3 sample that had the highest initial number of Mn^{3+} (layer plus interlayer). Samples initially equilibrated at pH 4–10 did not show evidence for transformation to cryptomelane, but had contrasting crystal chemistry ($\text{Na}_{0.12}^+(\text{H}_2\text{O})_{0.30}\text{Mn}_{0.315}^{3+}[\text{Mn}_{0.74}^{4+}\text{Vac}_{0.26}\text{O}_2]$ and $\text{Na}_{0.27}^+(\text{H}_2\text{O})_{0.30}\text{Mn}_{0.205}^{3+}[\text{Mn}_{0.79}^{4+}\text{Vac}_{0.21}\text{O}_2]$, respectively) after 8 years of ageing. The structure of pH 3 sample was not precisely determined, but crystals that transformed certainly had $\sim 1/3$ of $^{\text{TC}}\text{Mn}^{3+}$ per layer octahedron [49]. Still, many questions remain open as to the transformation mechanisms. In particular, it was unclear if the transformation was homogeneous at the crystal scale (if some crystals transformed to cryptomelane while others remained lamellar) or if it only affected portions of the crystals (topotactic transformation). Finally, tecto-manganates observed in natural environments are larger than typical vernadite [65, 66]. The mechanisms leading to crystal growth during or following vernadite to cryptomelane transformation (e.g., dissolution/recrystallization, aggregation, oriented attachment, Ostwald ripening) could not be elucidated.

The present study focuses further on the structure of aged $\delta\text{-MnO}_2$ samples studied by Grangeon and coworkers [49]. Samples that were initially equilibrated at pH values of 3, 4, 8, and 10, and then left ageing in the dark in the dry state for 10 years are hereafter referred to as $\text{MndBiXX}_{10\text{y}}$, where XX stands for the equilibration pH. These samples were selected because of their contrasting structures after 8 years of ageing (i.e., 2 years before the present study). $\text{MndBi3}_{10\text{y}}$ and $\text{MndBi10}_{10\text{y}}$ respectively represent the highest degree of transformation and an aged $\delta\text{-MnO}_2$ that retained its original lamellar structure. In the present study, synchrotron X-ray diffraction data is analyzed with both Bragg-rod and pair distribution function (PDF) methods to determine the sample structure as a function of pH, after two more years of ageing. Bragg-rod formalism is used to determine whether samples were partially transformed to cryptomelane, and to determine the size of coherent scattering domains (CSD)

and the number of $^{\text{TC}}\text{Mn}^{3+}$. PDF analysis is used to determine if layer vacancies are ordered and to cross-check the number of $^{\text{TC}}\text{Mn}^{3+}$. In addition, transmission electron microscopy (TEM) will be used to determine actual crystal sizes and to provide textural and structural constraints on the vernadite-to-cryptomelane transformation mechanisms. Scanning TEM will be used to reveal structural heterogeneities at the atomic scale.

Results

Analysis of X-ray diffraction patterns and Bragg-rod modeling

X-ray diffraction (XRD) patterns can be divided in two groups (Fig. 1). Patterns of $\text{MndBi8}_{10\text{y}}$ and $\text{MndBi10}_{10\text{y}}$ are typical for $\delta\text{-MnO}_2$, exhibiting reflections at 25.9 nm^{-1} (2.43 \AA), 44.3 nm^{-1} (1.42 \AA), and 51.3 nm^{-1} (1.22 \AA) that can be assigned to $[11, 20]$, $[31, 02]$, and $[22, 40]$ bands, using a C-centered unit cell with $\gamma = 90^\circ$ [67, 68].

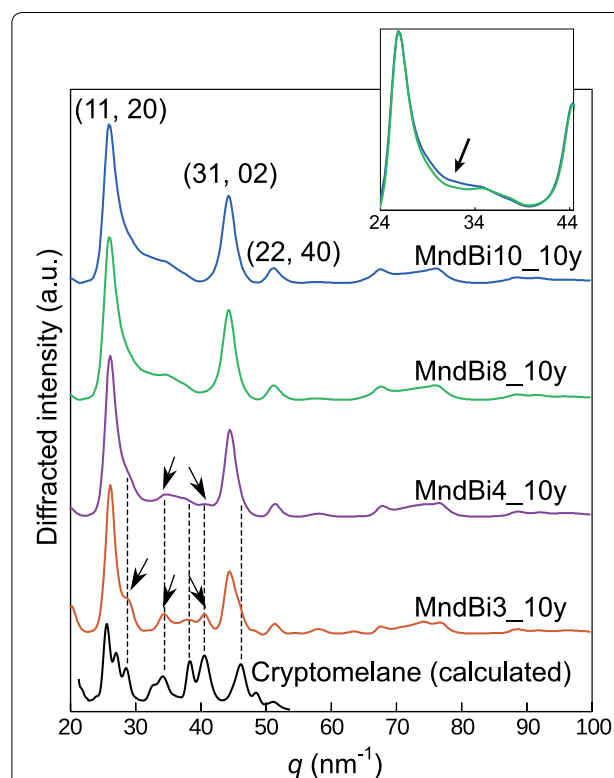


Fig. 1 XRD patterns of the studied samples and of a calculated cryptomelane pattern. *Main panel*, from top to bottom XRD patterns of $\text{MndBi10}_{10\text{y}}$, $\text{MndBi8}_{10\text{y}}$, $\text{MndBi4}_{10\text{y}}$, $\text{MndBi3}_{10\text{y}}$ and a calculated cryptomelane pattern (over the $21\text{--}53\text{ nm}^{-1}$ interval, CSD size of 6 nm). Patterns are scaled for clarity, as maximum intensity diffracted by $\delta\text{-MnO}_2$ is about 3 % of the maximum intensity diffracted by cryptomelane. *Arrows* point out to main modulations attributable to a cryptomelane-like structure in $\text{MndBi3}_{10\text{y}}$ and $\text{MndBi4}_{10\text{y}}$ patterns. $\text{MndBi10}_{10\text{y}}$ and $\text{MndBi8}_{10\text{y}}$ patterns are overlaid in the *inset* at the *top right* to highlight that the hump at $30\text{--}33\text{ nm}^{-1}$ is better defined in $\text{MndBi8}_{10\text{y}}$

Compared to MndBi10_10y, the hump at $30\text{--}33\text{ nm}^{-1}$ ($2.1\text{--}1.9\text{ Å}$) is better defined in MndBi8_10y (Fig. 1), likely as the result of a higher density of heavy interlayer species at TC sites. The symmetry and position of their $[31, 02]$ bands suggest that MndBi10_10y and MndBi8_10y both have hexagonal layer symmetry [67] and similar a and b unit-cell parameters [69]. CSD sizes along the c^* axis and layer-to-layer distance could not be determined owing to present experimental conditions that prevented modeling of low-angle $00l$ reflections.

Compared to MndBi8_10y and MndBi10_10y, additional reflections are observed at 29.0 nm^{-1} (2.17 Å), 34.4 nm^{-1} (1.83 Å), and 40.6 nm^{-1} (1.55 Å) in MndBi3_10y and MndBi4_10y. These reflections are more intense in MndBi3_10y than in MndBi4_10y (Fig. 1) and can be attributed to a cryptomelane-like structure. MndBi3_10y and MndBi4_10y are thus well-suited to study initial stages of the phyllomanganate-to-tectomanganate transformation, with part of MndBi3_10y and, to a lesser extent, of MndBi4_10y crystals having a cryptomelane-like structure.

Quantitative modeling of hk bands from MndBi8_10y and MndBi10_10y XRD patterns is shown in Fig. 2. Modeling of MndBi3_10y and MndBi4_10y patterns was not undertaken owing to the presence of cryptomelane, whose most intense reflections overlap $\delta\text{-MnO}_2$ [11, 20] band (Fig. 1). Relative intensity ratios calculated for cryptomelane and $\delta\text{-MnO}_2$ having similar CSD sizes ($\sim 6\text{ nm}$) indicate that cryptomelane represent $<5\%$ of the crystalline phases in the sample. MndBi10_10y has a CSD size in the ab plane of 5.8 nm and contains $0.11(1)\text{ }^{55}\text{Mn}^{3+}$ per layer octahedron (Table 1), lower than the value obtained 2 years sooner $[0.165(10)\text{ per layer octahedron}]$. Similar decrease of $^{55}\text{Mn}^{3+}$ with time was previously observed [70] and attributed to $^{55}\text{Mn}^{3+}$ to Mn^{4+} oxidation with time, followed by migration to the layer. This phenomenon may also be at play in other samples but could not be identified either because the structures were not refined (MndBi3_10y and MndBi4_10y) or because the structure of the same sample was not determined 2 years sooner owing to a restricted amount of sample available for analysis with conventional XRD instruments (MndBi8_10y). Finally, the number of interlayer H_2O molecules in MndBi10_10y was refined to 0.12 per interlayer site, slightly more than 2 years sooner (0.10). MndBi8_10y has CSD size in the ab plane of 6.2 nm , contains 0.02 more $^{55}\text{Mn}^{3+}$ and 0.02 more layer vacancies per layer octahedron than MndBi10_10y.

Analysis of PDF data

As PDF analysis will hereafter focus on short-range order, MndBi3_10y and MndBi4_10y, which contain a minor amount of cryptomelane, will be treated as pure $\delta\text{-MnO}_2$ owing to the structural similarities between the two

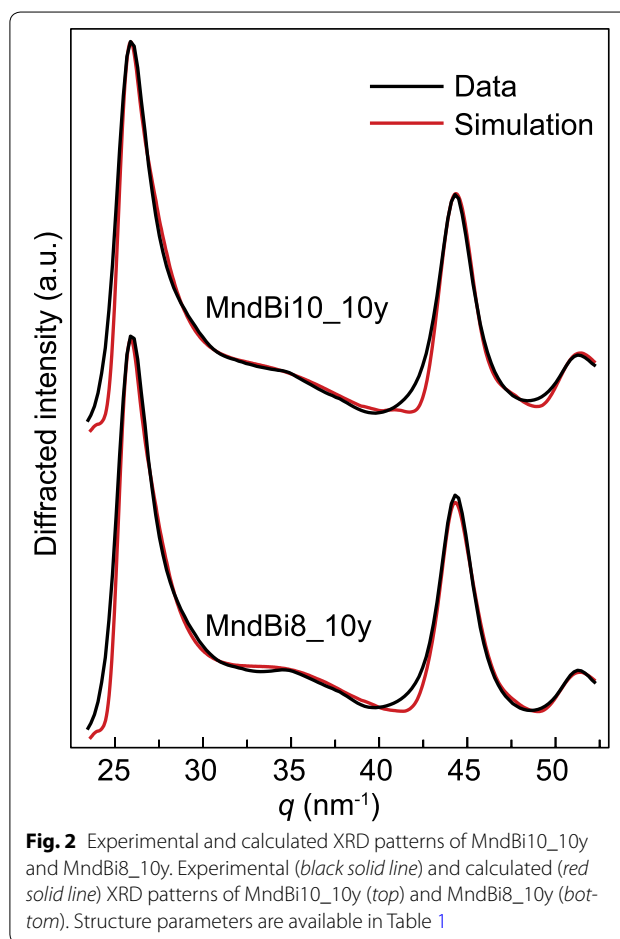


Fig. 2 Experimental and calculated XRD patterns of MndBi10_10y and MndBi8_10y. Experimental (black solid line) and calculated (red solid line) XRD patterns of MndBi10_10y (top) and MndBi8_10y (bottom). Structure parameters are available in Table 1

species. Indeed, Mn–Mn pairs from $\delta\text{-MnO}_2$ layers are similar to those in cryptomelane walls or floor/ceiling, and pairs formed by layer Mn and ^{55}Mn in $\delta\text{-MnO}_2$ are similar to those formed by Mn atoms from adjacent walls and floor/ceiling in cryptomelane. An implication of this similarity is that PDF data cannot be used, in the present study, to detect a minor amount of cryptomelane in the samples.

From a qualitative examination of the PDF data (Fig. 3), a systematic evolution is observed with sample equilibration pH. From MndBi10_10y to MndBi3_10y, correlations at $2.87, 4.95, 5.72,$ and 7.56 Å decrease in intensity (although the third appears less affected). These correlations are attributed to atomic pairs involving two layer Mn atoms and forming the first, second, third, and fourth Mn shells around a given layer Mn ($\text{Mn}\text{--}\text{Mn}_{\text{L}1}$, $\text{Mn}\text{--}\text{Mn}_{\text{L}2}$, $\text{Mn}\text{--}\text{Mn}_{\text{L}3}$ and $\text{Mn}\text{--}\text{Mn}_{\text{L}4}$ shells—Fig. 4a). Contrastingly, correlations at 3.45 and 5.32 Å increase in intensity. They are attributed to pairs formed by a layer Mn atom and a ^{55}Mn ($\text{Mn}\text{--}^{55}\text{Mn}$ pairs—Fig. 4b), with ^{55}Mn at vacancies belonging respectively to the first ($\text{Mn}\text{--}^{55}\text{Mn}_{\text{L}1}$) and second ($\text{Mn}\text{--}^{55}\text{Mn}_{\text{L}2}$) Mn–Mn_L

Table 1 Main structural parameters extracted from analysis of high energy X-ray scattering data, in the PDF and Bragg-rod approaches

Sample	^{55}Mn (per layer octahedron)		b (Å) ^a		c (Å)
	From PDF	From Bragg-rod	From PDF	From Bragg-rod	From PDF
MndBi3_10y	0.28(1)	n.d.	2.854(1)	n.d.	7.13(1)
MndBi4_10y	0.19(2)	n.d.	2.853(4)	n.d.	7.15(3)
MndBi8_10y	0.12(2)	0.13 (1)	2.868(4)	2.855	7.16(3)
MndBi10_10y	0.09(2)	0.11 (1)	2.869(4)	2.855	7.18(3)

Anisotropic Debye–Waller factors, as well as other fit parameters, determined from PDF analysis, are available in Additional file 1: Data S1. Uncertainties on results from PDF simulation is indicated under brackets, and represents the uncertainty on the value of the last digit

^a a was constrained to be equal to $\sqrt{3}b$

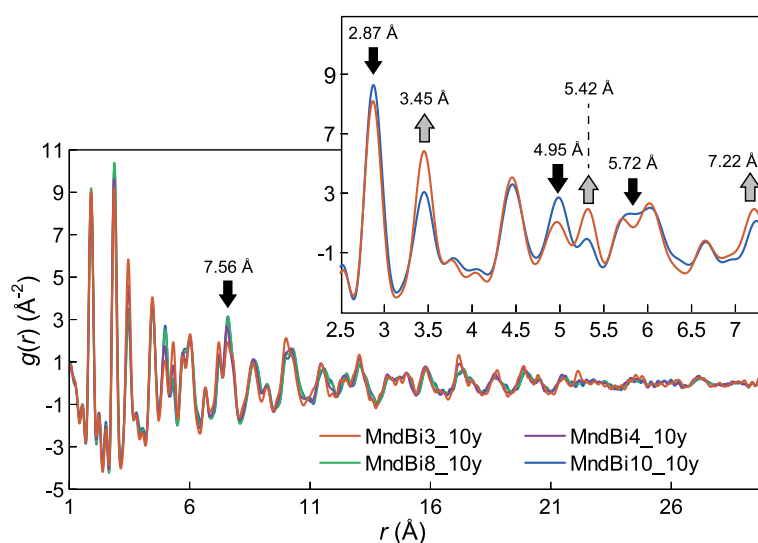


Fig. 3 Comparison of PDF of all studied samples. *Main panel* PDF of MndBi3_10y (orange), MndBi4_10y (purple), MndBi8_10y (green) and MndBi10_10y (blue). *Inset at the top right* shows alternations of decreasing (black arrows) and increasing (grey arrows) correlations, from MndBi10_10y to MndBi3_10y. Only MndBi10_10y and MndBi3_10y are shown in the inset to ease visualization

shells (Fig. 4a, b, c). The number of layer vacancies thus increases from MndBi10_10y to MndBi3_10y, ^{55}Mn being sorbed above these vacancies. The first, second and fourth Mn–Mn_L shells are more affected than the third shell. All these shells contain, in a defect-free $\delta\text{-MnO}_2$ layer, 6 Mn atoms. Thus, a layer vacancy normally affects equally all of these shells, and the observed behavior can most straightforwardly be explained by an ordered layer vacancy distribution. Finally, the correlation at 7.22 Å increases in intensity from MndBi10_10y to MndBi3_10y. It corresponds to a ^{55}Mn – ^{55}Mn pair, with ^{55}Mn atoms being on opposite sides of layer vacancies separated from each other by one layer Mn atom (^{55}Mn – $^{55}\text{Mn}_1$ in Fig. 4c). All these correlations and in particular the ^{55}Mn – ^{55}Mn one are typical for $\delta\text{-MnO}_2$ layers having 0.25 layer vacancy per layer octahedron and

^{55}Mn as in Fig. 4c. In addition, the correlation at 6.13 Å (Mn– $^{55}\text{Mn}_3$ pair, i.e., ^{55}Mn above a vacancy belonging to the Mn–Mn_{L3} shell) may indicate the minor presence of domains with 0.33 vacancy per layer octahedron in low pH samples (Fig. 4d). Such domains could correspond to the cryptomelane-like structure or to their precursors.

As discussed hereafter and by Manceau and coworkers [70], $\delta\text{-MnO}_2$ PDF data are affected by sample turbostratism, that is by the systematic presence of random translation and/or rotation between successive layers. Turbostratism decreases the intensity of correlations for r values higher than the layer-to-layer distance, because coherency between adjacent layers is lost. In the present samples both ~ 7.2 and ~ 10 Å layer-to-layer distances were observed (see below), the former being by far the most frequent. As a consequence,

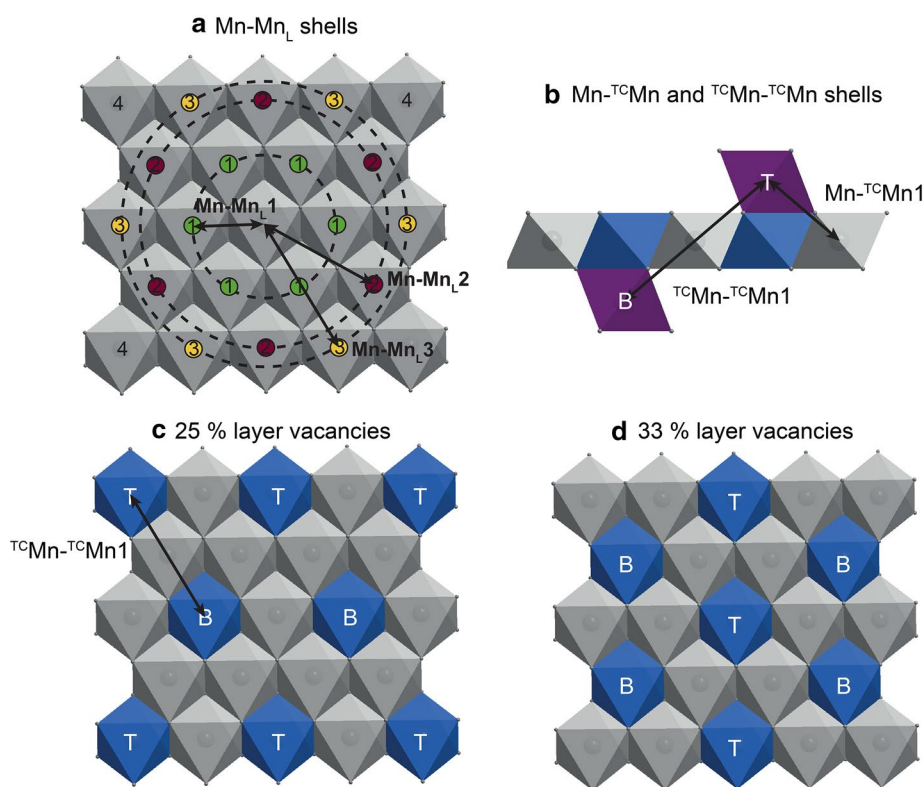


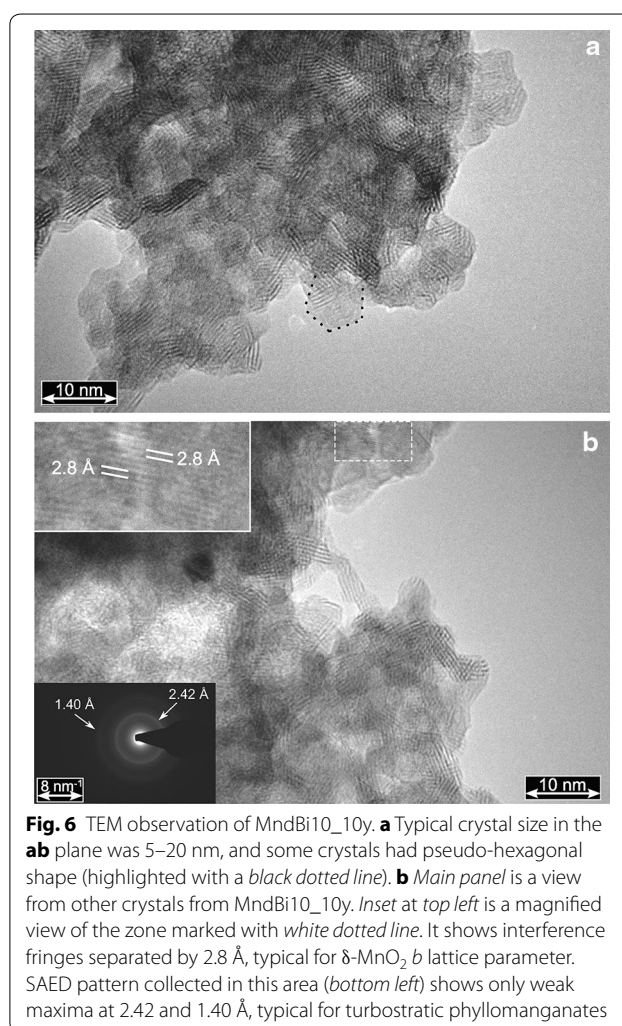
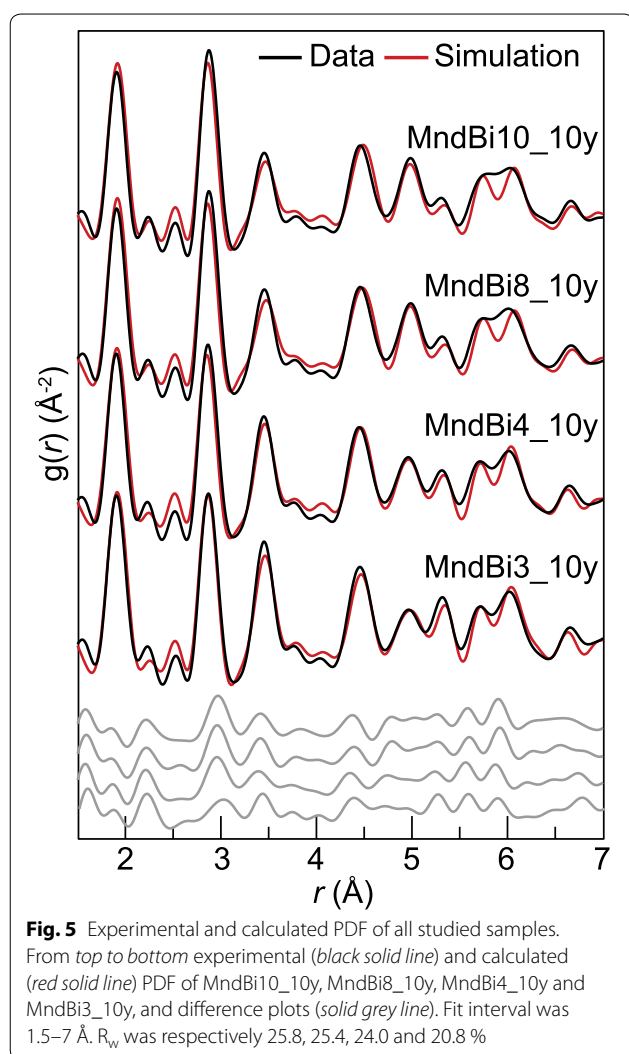
Fig. 4 Scheme of vernadite layer and of atomic pairs involving Mn atoms. **a** Scheme of a vernadite layer, seen along c^* with grey octahedra representing $(\text{MnO}_6)^{8-}$ octahedra. The first three atomic shells formed by layer Mn around a given layer Mn ($\text{Mn-Mn}_L\text{X}$ pairs, where X stands for the atomic shell) are highlighted with concentric circles. Green full circles with a “1” mark, red full circles with a “2” mark, orange full circles with a “3” mark, and “4” marks respectively schematize layer Mn belonging to the first, second, third and fourth (only partly represented) atomic shells. **b** Scheme of a layer seen perpendicular to c^* . Blue octahedra are layer vacancies, which are capped on one side by $^{\text{TC}}\text{Mn}^{3+}$ (purple octahedra). The first layer Mn to $^{\text{TC}}\text{Mn}$ pair ($\text{Mn-}^{\text{TC}}\text{Mn1}$) as well as the first $^{\text{TC}}\text{Mn}$ to $^{\text{TC}}\text{Mn}$ pair, when the two atoms are on opposite sides of the layer ($^{\text{TC}}\text{Mn-}^{\text{TC}}\text{Mn1}$), are represented. “T” stands for “top” and means that a $^{\text{TC}}\text{Mn}$ is located on the other side of the layer as compared to a $^{\text{TC}}\text{Mn}$ labeled “B” (standing for “bottom”). **c** Scheme of a layer containing 1/4 vacancy (blue octahedra) per layer octahedron, vacancies being ordered. Purple octahedra are omitted for clarity, only the captions “T” and “B” are left to materialize $^{\text{TC}}\text{Mn}$. The first $^{\text{TC}}\text{Mn-}^{\text{TC}}\text{Mn}$ pair is highlighted with arrows. **d** Same as **c**, but with a layer containing 1/3 vacancy per layer octahedron

refinement was restricted to the 1.5–7 Å intra-layer interval which is not affected by turbostratism. The model from Manceau and coworkers [70] was used and no attempt was made to refine atomic coordinates nor layer symmetry. Refined parameters corresponding to the simulations shown in Fig. 5 are reported in Table 1 and Additional file 1: Data S1. With decreasing pH, the abundance of $^{\text{TC}}\text{Mn}^{3+}$ steadily increased, from 0.09(2) per layer octahedron in $\text{MndBi10}_{10\text{y}}$ to 0.28(1) per layer octahedron in $\text{MndBi3}_{10\text{y}}$ (Table 1), consistent with previous studies [49, 70, 71]. Layer parameters decreased from $b = 2.869(4)$ Å in $\text{MndBi10}_{10\text{y}}$ to $b = 2.854(1)$ Å in $\text{MndBi3}_{10\text{y}}$, certainly as a result of the increase in $^{\text{TC}}\text{Mn}^{3+}$ [49]. These values are systematically lower [0.013(4)–0.014(4) Å] than those obtained using the Bragg-rod approach (Table 1) possibly as a consequence of layer bending [70].

Morphological and structural evolution with pH as seen by transmission electron microscopy

Bragg-rod and PDF data analysis allowed probing structure of coherent scattering domains but could not determine their distribution within crystals, and in particular the possible coexistence of $\delta\text{-MnO}_2$ and cryptomelane domains within crystals. As they are representative of samples undergoing the maximum and minimum degree of structural conversion, $\text{MndBi3}_{10\text{y}}$ and $\text{MndBi10}_{10\text{y}}$ were investigated by TEM to gain further insights into transformation mechanisms.

$\text{MndBi10}_{10\text{y}}$ was composed of crystals having homogenous size and morphology, often found aggregated in a xerogel-like configuration. Selected area electron diffraction (SAED) patterns were typical for $\delta\text{-MnO}_2$, with two broad diffraction maxima at ~ 2.42 and ~ 1.40 Å (Fig. 6) that correspond to [11, 20] and [31, 02] diffraction bands.

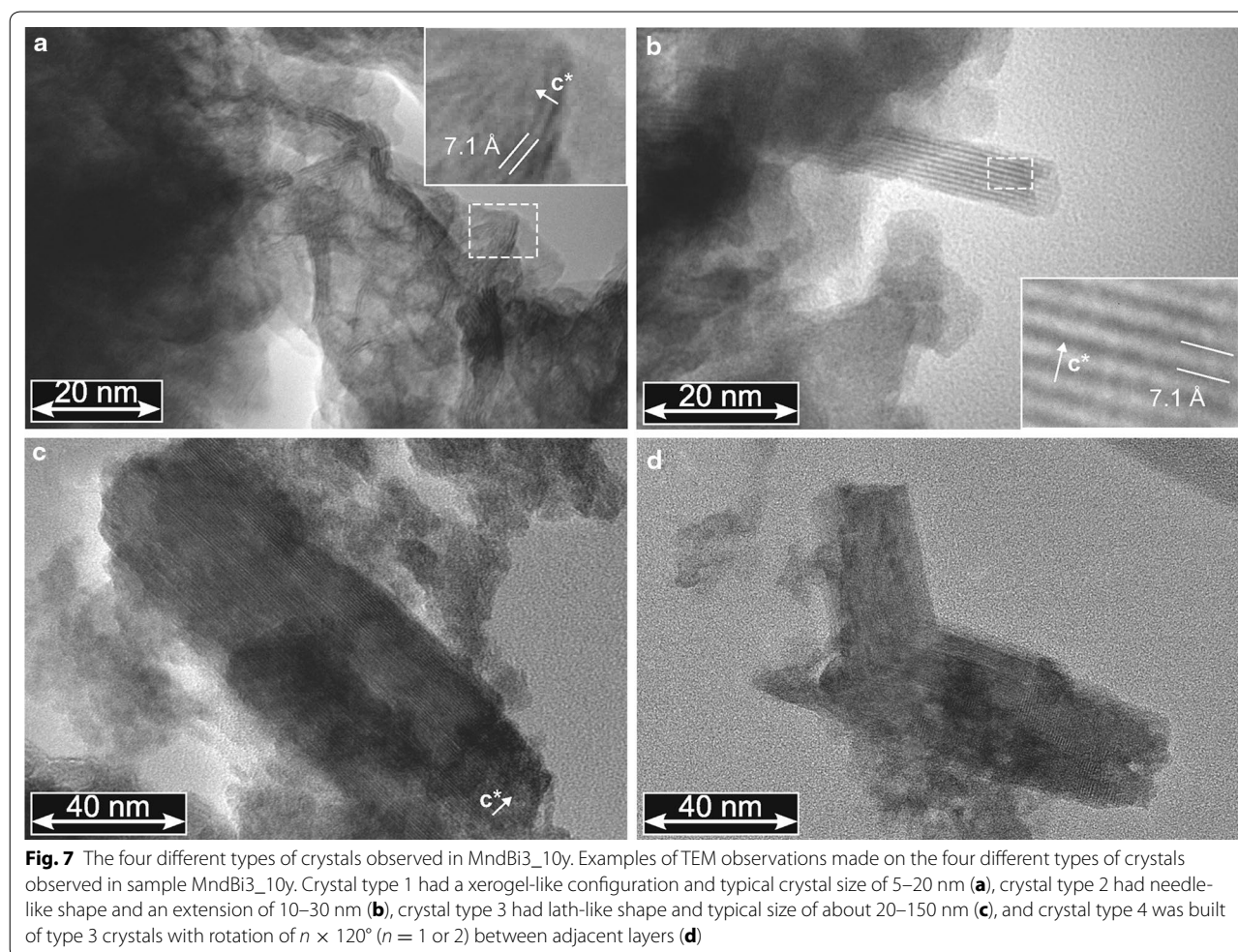


Crystal sizes in the **ab** plane range 5–10 nm, consistent with CSD size determined from XRD pattern modeling (5.8 nm). Some crystals exhibited hexagonal shape in the **ab** plane (Fig. 6a), as observed in other δ -MnO₂ samples [45, 70]. Finally, interference fringes having spacing of ~ 2.8 Å could be observed (Fig. 6b) and are attributed to the *b* parameter.

Observation of MndBi3_10y samples revealed a much more complex assemblage. The sample contained at least four types of crystals distinguishable on the basis of their morphology and size (Figs. 7, 8). Crystal type 1 had sizes of 5–20 nm, similar to fresh samples (data not shown) and MndBi10_10y. Crystal type 2 had a needle-like morphology, typically 10–30 nm in length. Crystal type 3 had lath-like morphology, with its long distance in the **ab** plane (20–150 nm) up to ~ 5 –10 times larger than crystal type 2. It was also typically 2–10 times wider, and interference fringes were frequently disrupted, as if it was

built of aggregated type 2 crystals (Fig. 9). Aggregation was observed to occur within the **ab** plane, in agreement with the aggregation mechanism proposed previously [50, 60, 72]. It was also observed along *c**, with disruption of interference fringes that had geometrical shapes identical to previous observations [60, 72, 73] and indicate that growth may also take place through stacking along *c** of two or more type 2 crystals. Finally, crystal type 4 often had typical sizes of 50–150 nm in the **ab** plane and 10–50 nm along *c**, and was built of stacks of lath-like layers resembling type 3 crystals rotated by $n \times 120^\circ$ (*n* being equal to 1 or 2) relative to each other.

Similar to MndBi10_10y, crystal type 1 in MndBi3_10y exhibited SAED patterns typical for δ -MnO₂, with only weak diffraction maxima at 2.42 and 1.40 Å (Fig. 8). Contrastingly, crystal type 4 exhibited additional reflections (e.g., at 2.19, 1.80, and 1.54 Å—Fig. 8) attributed to cryptomelane. Consequently, MndBi3_10y is built of four main types of crystals: crystal type 1 is a



phylломanganate, whereas crystal type 4 locally has a tectomanganate-like structure. We propose that crystals type 2 and 3, that could not be investigated by SAED as no isolated crystal or homogeneous aggregate could be found, have an intermediate structure. When viewed perpendicular to the c^* axis, crystal type 4 systematically showed the presence of tunnel-like structures, with sizes of $6.9 \text{ \AA} \times 6.9 \text{ \AA}$ typical for cryptomelane (Fig. 10). The minor presence of heterogeneous tunnel size (dotted arrows in Fig. 10) is likely. Finally, analysis of images collected on type 1, 2 and 3 crystals (Figs. 7a, b, 9) reveal distances of $\sim 6.9\text{--}7.1 \text{ \AA}$, consistent with layer-to-layer distance of phylломanganates hosting a single plane of interlayer H_2O molecules. 9.5 \AA distances expected for phylломanganates hosting two planes of water molecules [74] were also observed, although much less frequent. This uncommon persistence of highly hydrated states under TEM vacuum conditions [60, 75] is likely related to sample impregnation in resin prior to analysis.

Additional high-resolution STEM image was obtained at 100 keV (Fig. 11) to minimize structure evolution

under the electron beam and to improve resolution in an effort to investigate the possible segregation of heterovalent Mn cations. Consistent with TEM observations (Fig. 10), $[2 \times 3]$ tunnels were observed in crystal type 4 together with prevailing $[2 \times 2]$ tunnels size, with individual Mn atoms being clearly observed. The latter tunnels have contrasting floor/ceiling and wall dimensions, with their small dimension (supposedly the former phylломanganate layers) $\sim 5 \%$ smaller than the perpendicular dimension (Fig. 11c). This supports the hypothesis of Mn^{3+} atoms (that have a larger distorted coordination octahedron) segregation in the walls whereas Mn^{4+} atoms are mainly present in tunnel floors and ceilings. Finally, the structure was found to suffer from bending (Fig. 11d).

Discussion

Mechanism of the phylломanganate to tectomanganate transformation

To our knowledge, this study is the first to document the transformation of vernadite to cryptomelane under

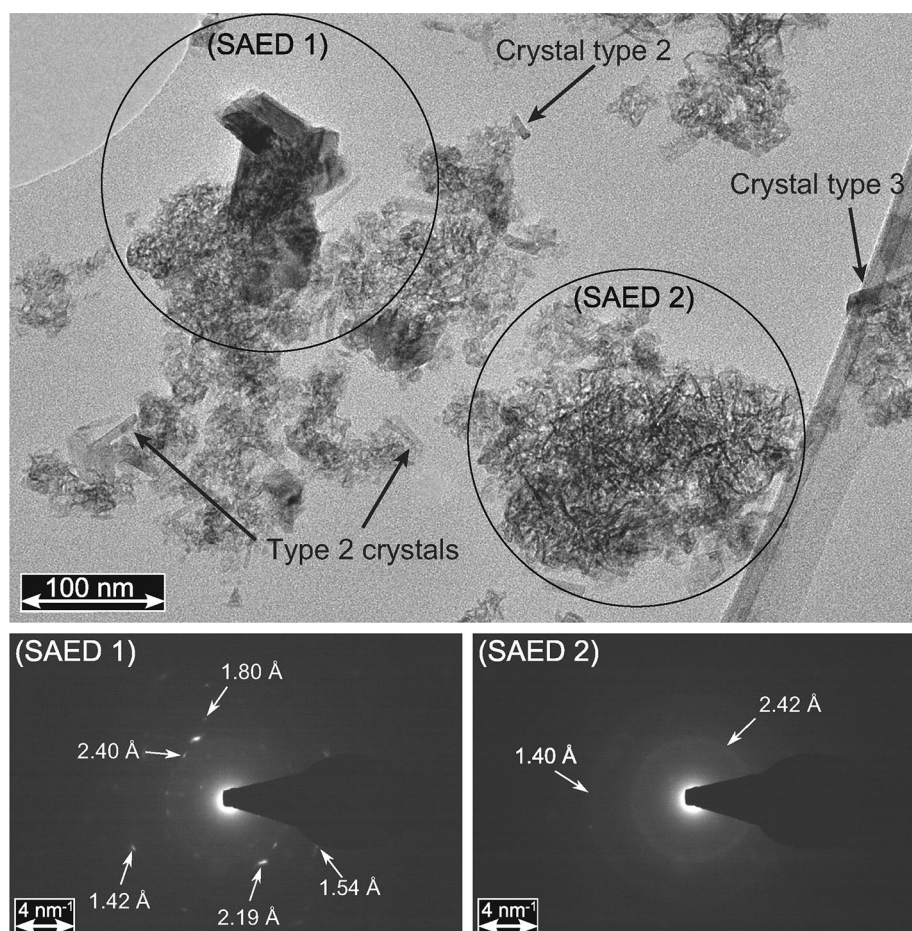
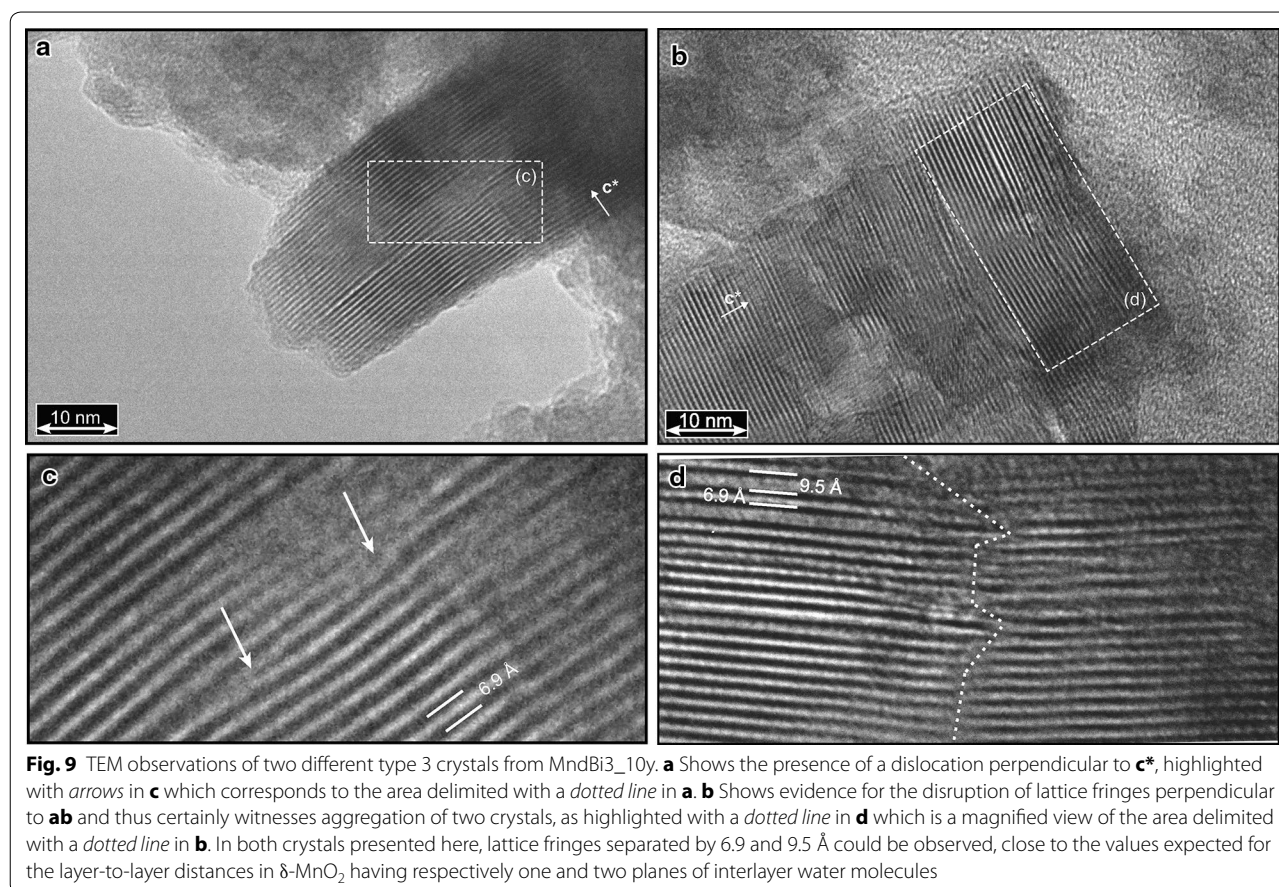


Fig. 8 TEM observation of MnDBi3_10y and SAED patterns of type 1 and type 4 crystals. *Top panel* Low-magnification view of crystals from MnDBi3_10y. Circles indicate areas which were subjected to electron diffraction. Circle at the *top left* (SAED 1) targeted crystal type 4, which had a diffraction pattern exhibiting features characteristics for cryptomelane, and in particular d -spacing of 2.40, 2.19, 1.80, 1.54 and 1.42 Å (pattern at the *bottom left*). Circle at the *bottom right* (SAED 2) targeted crystal type 1 and had a signal typical for δ -MnO₂, with distances of 2.42 and 1.40 Å (pattern at the *bottom right*). Crystals types 2 and 3 which are most easily distinguishable are pointed out with arrows

conditions that can be considered relevant for soils, i.e. at room temperature, $\sim 10^5$ Pa, under unsaturated conditions, and in the dark. As previously discussed [49], this structural transformation requires a locally high number of Mn³⁺ (~ 0.33 per layer octahedron) in the octahedral layer. This can be obtained experimentally by equilibrating phyllosulfates at low pH values (≤ 4) that can be observed in forest soils, soils developed on parent granite or gneiss, or organic-rich soils [76]. Such assumption is confirmed by independent laboratory experiments which show that δ -MnO₂ to cryptomelane transformation is favored at low pH [72].

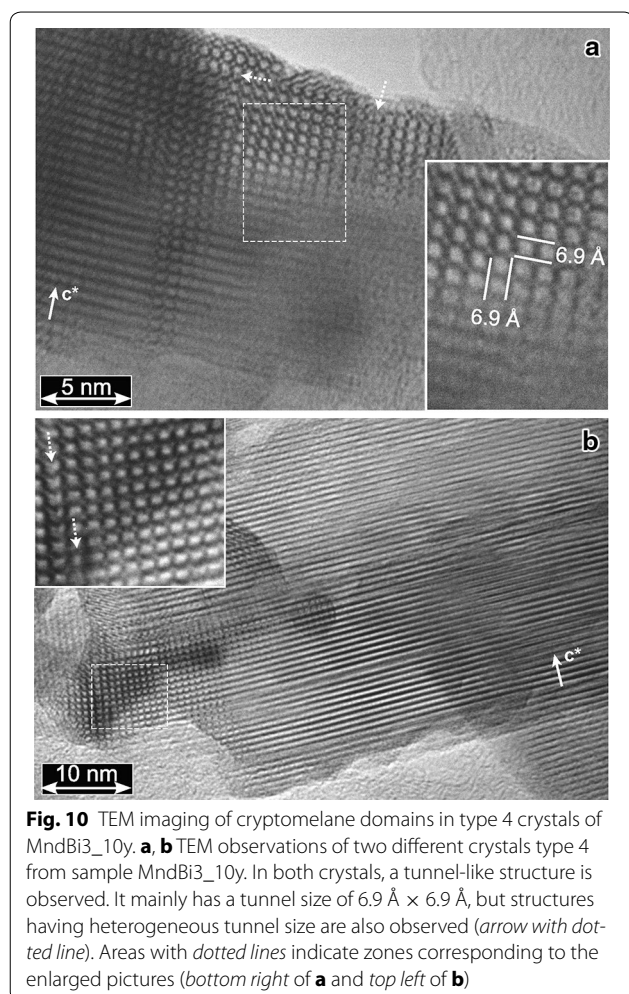
From many viewpoints, the studied transformation is similar to that of δ -MnO₂ to todorokite described by Atkins and coworkers [60]. The contrasting reaction products obtained in the two studies are most likely due

to the different nature of interlayer cation in the initial phyllosulfate (Na⁺ in the present study and Mg²⁺ for Atkins and coworkers). The first reaction step differs however as Atkins and coworkers propose that the presence of layer Mn³⁺ leads to layer kinking, owing to their Jahn–Teller distorted coordination sphere. In our opinion, reaction first step rather corresponds to the migration of Mn³⁺ from the layer to the interlayer, which allows also releasing strains related to the Jahn–Teller distortion of Mn³⁺ octahedra. This interpretation is consistent with the infrared data of Atkins and coworkers that showed an increased density of ⁵⁵Mn during the initial steps of the transformation. The proposed mechanism accounts also for their observation, corroborated by Feng and coworkers [53], that transformation occurs at constant mean Mn oxidation degree. In contrast to



the hypothesis of Atkins and coworkers this initial step is likely not thermally triggered but reaction kinetics is enhanced with increasing temperature. The next steps of the reaction described by Atkins and coworkers are also observed in the present study. Needle-like crystal type 2 results indeed from the crystal growth along tectomanganate tunnels proposed by Atkins and coworkers, whereas lath-like crystal type 3 results from crystal growth perpendicular to tectomanganate tunnels (by coalescence of type 2 crystals along their long dimension). Finally, crystal type 4, built of lath-like units rotated by $n \times 120^\circ$ (n being equal to 1 or 2), results from stacking of crystal type 3. The crystallographic axes along which crystal growth/aggregation takes place could not be determined in the present study, as SAED patterns could not be collected on type 2 and 3 crystals, and as instrumental limitations hampered the observations of in-plane lattice fringes. A last transformation step was described by Atkins and coworkers as Ostwald ripening and would involve cryptomelane crystal growth. This final step could not be observed in the present samples as evidence for a cryptomelane-like signal could only be found in crystal type 4 (Fig. 8). To date, only Bodei and coworkers [46] have investigated in detail the mechanisms

of phyllomanganate (vernadite) to tectomanganate (todorokite) transformation in natural samples. Collation of the present study with that of these authors is hampered however by numerous unknowns inherent to natural systems, such as the density of layer and interlayer Mn^{3+} in the initial phyllomanganate and the structural variety of natural tectomanganates [77, 78]. However, several clues suggest that the observed transformation is similar to that occurring in natural systems. First, proposed transformation mechanisms are valid both in surface soil conditions (present study) and in saturated conditions [50, 72], making them relevant to a variety of natural systems. Second, naturally occurring tectomanganates frequently exhibit textures similar to those observed in experimental studies (Figs. 7, 8; [51, 53, 60, 79, 80]) with rotations of aggregated crystals by $n \times 120^\circ$ [46, 66, 79]. Third, transformations occur via topotactic transformation in both experimental and natural systems and are heterogeneous at the crystal scale. In particular, transformation systematically affects only part of the crystals and the transformed parts show heterogeneous tunnel sizes. This latter point is certainly related to an imperfect distribution of Mn^{3+} atoms ($^{55}Mn^{3+}$ + layer Mn^{3+}) in the initial phyllomanganate structure.



Conclusion

The phyllosilicate-to-tectomanganate transformation (Fig. 12) was studied using a combination of high-energy X-ray scattering and transmission electron microscopy. It was confirmed that this transformation is triggered when the number of $^{TC}Mn^{3+}$ locally reaches ~ 0.33 per layer octahedron. The possible influence of Mn^{4+} to Mn^{3+} photo-reduction [81] on the transformation remains to be investigated. Part of $^{TC}Mn^{3+}$ cations result from the migration of layer Mn^{3+} to the interlayer, which demonstrates that prediction of vernadite to tectomanganate transformation requires a sound understanding of vernadite structure, including quantification of both $^{TC}Mn^{3+}$ and layer Mn^{3+} in starting material. In addition, the nature of the tectomanganate that will be formed is dependent on the nature of the interlayer cation: if the cation is capable of enforcing a 10 Å layer-to-layer distance, todorokite will be formed; otherwise, the product of reaction will be cryptomelane.

Growth mechanisms proposed from previous experimental studies performed at higher temperatures were confirmed for conditions relevant to surface soil. The four-stage transformation begins with the migration of Mn^{3+} from layer to the interlayer to form $^{TC}Mn^{3+}$ that further connect to hydration spheres belonging to $^{TC}Mn^{3+}$ from adjacent layers. Crystals then grow first along the “tunnel” direction to form needle-like crystals. These crystals coalesce along their long dimension to form lath-like crystals which, in a final step, stack along c^* with rotation by $n \times 120^\circ$ between adjacent laths. Cryptomelane structure was observed only in these latter crystals (type 4), but is certainly present also in crystals type 2 and 3.

Methods

Samples investigated

Samples used for the present study are those studied by Grangeon and coworkers [49] and Manceau and coworkers [70]. They were synthesized using the redox method [2] and were left for equilibration at pH values ranging from 3 to 10 immediately after synthesis. They were then left to age for 10 years in the dark and in the dry state. For consistency with Grangeon and coworkers [49], samples are labeled MndBiXX_10y, where XX is the equilibrium pH and “10y” stands for “10 years of ageing”.

X-ray diffraction pattern (XRD) analysis and modeling

XRD patterns were modeled using the software developed by Plançon [82], based on the formalism developed by Drits and Tchoubar [83]. This specific routine allows for the simulation of (lamellar) structures affected by various nature and density of layer defects (e.g., layer vacancies, isomorphic substitutions) and stacking defects (e.g., well-defined or random stacking faults, interstratification). It has been previously applied to the study of nanocrystalline manganese or iron oxides [69, 84, 85], nanocrystalline calcium silicate hydrates [86–88] and phyllosilicates [89, 90]. As discussed by Manceau and coworkers [70] the simulation of the [11, 20], [31, 02] and [22, 40] bands (using a C-centered hexagonal unit-cell, with $\gamma = 90^\circ$) is sufficient to accurately determine the structure of synthetic phyllosilicates, and only these bands were modeled here. All structure parameters but crystallite size, a and b lattice parameters, abundance of $^{TC}Mn^{3+}$, layer vacancies and of interlayer water molecules were kept identical to those determined by Grangeon and coworkers [49]. An example of the sensitivity of calculated XRD patterns to the number of $^{TC}Mn^{3+}$ is available in the Additional File 2: Data S2. The cryptomelane pattern was calculated using the structure model from Vicat and coworkers [91], assuming a CSD size of 6 nm.

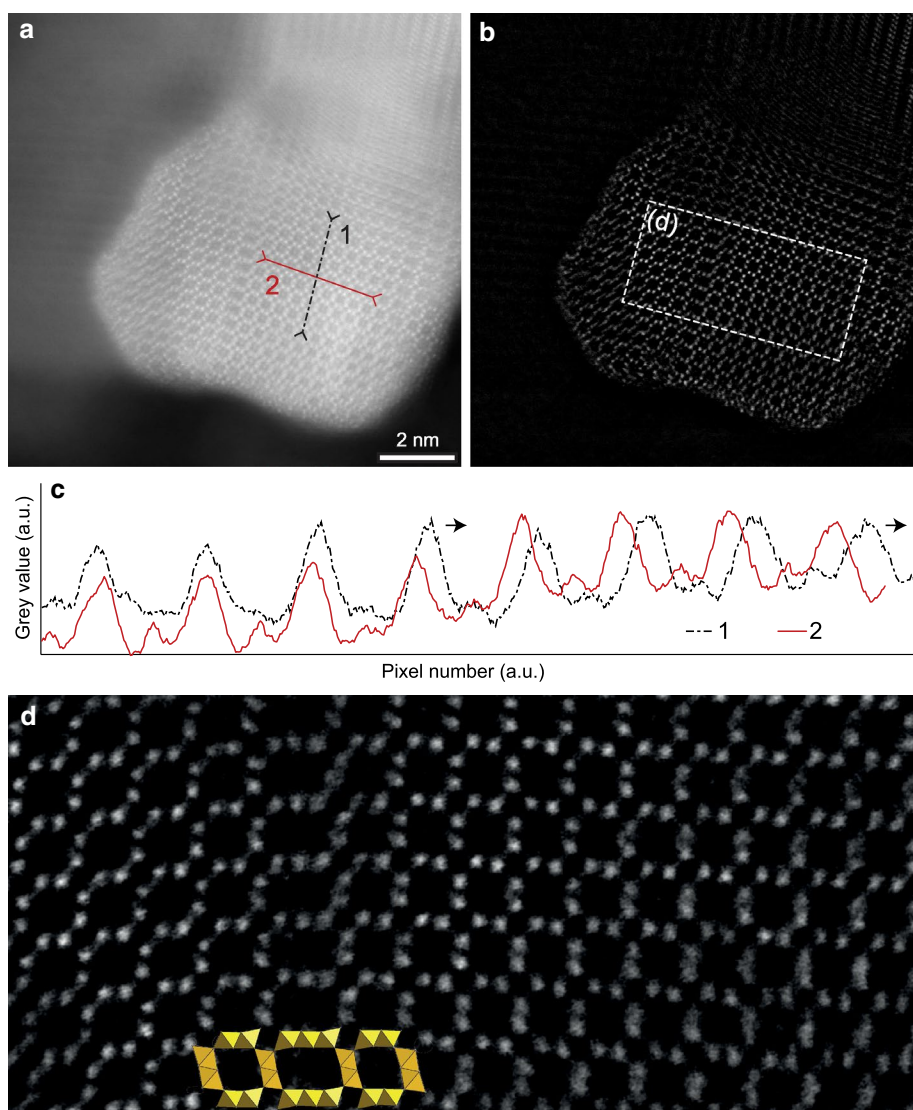
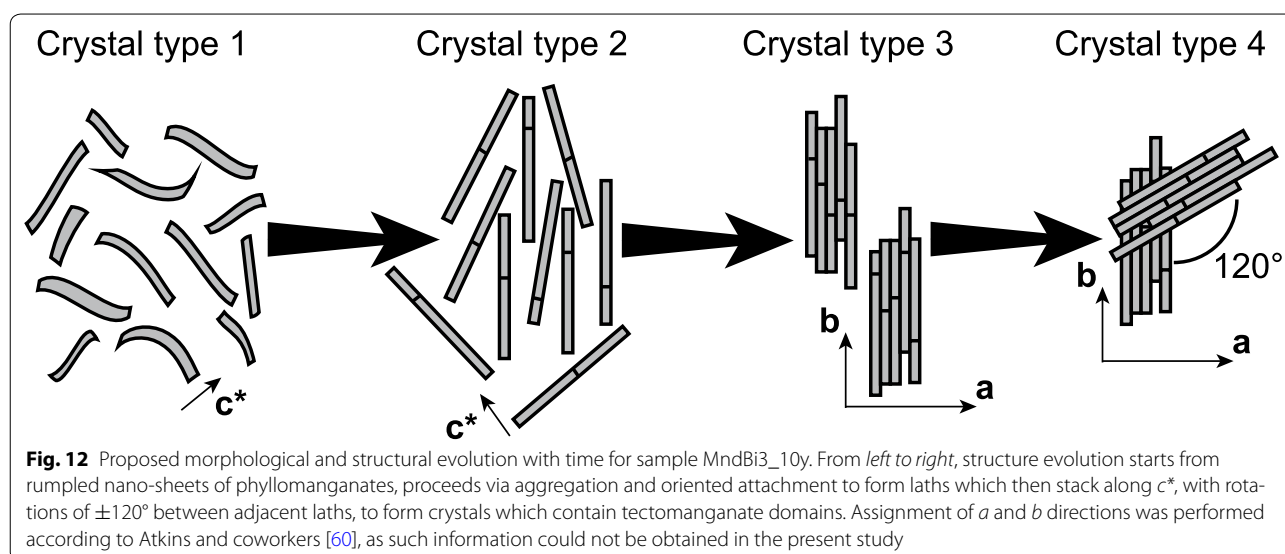


Fig. 11 STEM imaging of a cryptomelane domain in crystal type 4 of $\text{MndBi3}_{10\text{y}}$. **a** STEM observation of a cryptomelane domain in $\text{MndBi3}_{10\text{y}}$. Electron density is maximum when color is *white*, and minimum when color is *black*. **b** Is the same image after post-processing. Most of the particle is made of $[2 \times 2]$ tunnel structures, but $[3 \times 2]$ structures are also visible. **c** Shows the pixel *grey* values in two transects (delimited in **a**) along and perpendicular to tunnel walls. *Arrows* highlight the phase shift occurring between the two signals and thus the difference in tunnel size parallel and perpendicular to the tunnel walls. **d** Is a magnified view of part of **b** (area delimited with a *dotted line* in **b**), with a sketch of $[2 \times 2]$ and $[2 \times 3]$ tunnel structures overlaid to ease interpretation

High energy X-ray scattering coupled with pair distribution function (PDF) analysis and modeling

X-ray diffraction patterns were collected at ID15B high-energy beamline of the European Synchrotron Radiation Facility (ESRF, Grenoble, France), using energy of 87 keV and a PerkinElmer flat panel detector. Data were acquired on randomly-oriented powders packed in polyimide capillaries having a diameter of 1 mm and on empty capillary used for background subtraction. 40 frames of 5 s, corrected for detector's dark current, were collected for

each sample. After instrumental calibration using a NIST certified CeO_2 powder sample, frames were integrated to one dimensional patterns [92] and averaged. Data were then transformed to PDF patterns using PdfGetX3 [93], and fit using PDFGui [94]. The model from Manceau and coworkers [70] was used to refine the patterns. The only modification was that $^{\text{TC}}\text{Mn}^{3+}$ was allowed to sorb on both sides of a layer vacancy. The refined parameters were the abundance of $^{\text{TC}}\text{Mn}^{3+}$, layer vacancies, lattice parameters and Debye–Waller factors. q broadening and



q damping factors were retrieved from simulation of a CeO_2 pattern and found to be equal to, respectively, 0.044 and 0.048.

Transmission electron microscopy (TEM)

TEM was performed using a Philips CM20 operated at 200 kV. Samples were deposited on a copper grid prior to observation. When samples were first dispersed in ethanol or in water, and deposited on the grid from the suspension, they were rapidly altered under the beam, with amorphous products occurring within a few seconds. To circumvent this problem, samples were first embedded in epoxy resin and left in the dark for 48 h until full polymerization. Cutting was performed using an ultramicrotome Reichert-Jung Ultra-cut E. Five to ten thin sections having thicknesses of about 100 nm were collected on the surface of the water contained in the boated knife and picked up on a lacey carbon film loaded on copper grids.

Scanning transmission electron microscopy (STEM)

STEM experiments were performed using a Nion Ultra-STEM 200 operated at 100 kV. Sample preparation was identical to that applied for TEM measurements, except that the thickness of the slices containing the sample embedded in epoxy resin was reduced to ~ 50 nm. Image presented in the present study was acquired in high-angular annular dark-field (HAADF) mode. In order to ease visualization of the structural features, the raw image was Fourier-transformed and filtered using a band pass with a window set for spatial frequencies between 1.6 and 40 nm^{-1} , and a color threshold was then applied to reduce the contribution from pixels having a grey color lower than half of the mean image grey value.

Additional files

Additional file 1: Data S1. A table listing all parameters, but those listed in Table 1, which were refined during PDF data analysis.

Additional file 2: Data S2. The sensitivity of calculated XRD patterns to the number of $^{55}\text{Mn}^{3+}$.

Authors' contributions

AFM, AP, SG and NM participated to high-energy X-ray scattering experiments (HEXS). SG processed HEXS data. FW and SG did TEM experiments. SG and FW processed and analyzed TEM data. AG conducted STEM experiments to which FW and SG participated. AG, FW and SG interpreted STEM data. SG wrote the main parts of the manuscript. AFM, FW, NM, AG and BL participated to manuscript writing. All authors read and approved the final manuscript.

Author details

¹ BRGM, 3 Avenue Guillemin, 45060 Orléans Cedex 2, France. ² Univ. Grenoble Alpes, ISTERRE, 38041 Grenoble, France. ³ CNRS, ISTERRE, 38041 Grenoble, France. ⁴ ICMN-CNRS-Université D'Orléans, 1b rue de la Férollerie, 45071 Orléans Cedex 2, France. ⁵ Laboratoire de Physique des Solides, Université Paris-Sud, CNRS, UMR 8502, 91405 Orsay Cedex, France. ⁶ ESRF-The European Synchrotron, 71 avenue des Martyrs, Grenoble, France.

Acknowledgements

S.G. acknowledges funding from the ANR (NACRE—ANR-14-CE01-0006). AFM was supported by a grant from Labex OSUG@2020 (Investissements d'avenir—ANR10 LABX56). Synchrotron experiments were performed on the ID15B beamline at the European Synchrotron Radiation Facility (ESRF), Grenoble, France. STEM experiments were performed at the LPS (Laboratoire de Physique des Solides, Orsay, France) in the frame of a research project granted to SG and FW by the national network for transmission electron microscopy and atom probe studies in France (METSA). This article benefited from comments and suggestions made by two anonymous reviewers and by Xionghang Feng (associate editor).

Compliance with ethical guidelines

Competing interests

The authors declare that they have no competing interests.

Received: 22 January 2015 Accepted: 14 August 2015

Published online: 02 September 2015

References

- Jürgensen A, Widmeyer JR, Gordon RA, Bendell-Young LJ, Moore MM, Crozier ED (2004) The structure of the manganese oxide on the sheath of the bacterium *Leptothrix discophora*: an XAFS study. *Am Miner* 89:1110–1118
- Villalobos M, Toner B, Bargar J, Sposito G (2003) Characterization of the manganese oxide produced by *Pseudomonas putida* strain MnB1. *Geochim Cosmochim Acta* 67:2649–2662
- Webb SM, Tebo BM, Bargar JR (2005) Structural characterization of biogenic Mn oxides produced in seawater by the marine *Bacillus sp.* strain SG-1. *Am Miner* 90:1342–1357
- Grangeon S, Lanson B, Miyata N, Tani Y, Manceau A (2010) Structure of nanocrystalline phyllosulfates produced by freshwater fungi. *Am Miner* 95:1608–1616
- Miyata N, Maruo K, Tani Y, Tsuno H, Seyama H, Soma M, Iwahori K (2006) Production of biogenic manganese oxides by anamorphic ascomycete fungi isolated from streambed pebbles. *Geomicrobiol J* 23:63–73
- Tani Y, Miyata N, Iwahori K, Soma M, Tokuda S-I, Seyama H, Theng BKG (2003) Biogeochemistry of manganese oxide coatings on pebble surfaces in the Kikukawa River System, Shizuoka, Japan. *Appl Geochem* 18:1541–1554
- Lanson B, Marcus MA, Fakra S, Panfil F, Geoffroy N, Manceau A (2008) Formation of Zn–Ca phyllosulfate nanoparticles in grass roots. *Geochim Cosmochim Acta* 72:2478–2490
- Crerar DA, Barnes HL (1974) Deposition of deep-sea manganese nodules. *Geochim Cosmochim Acta* 38:279–300
- Morgan JJ (2005) Kinetics of reaction between O₂ and Mn(II) species in aqueous solutions. *Geochim Cosmochim Acta* 69:35–48
- Tebo BM, Bargar JR, Clement BG, Dick GJ, Murray KJ, Parker D, Verity R, Webb SM (2004) Biogenic manganese oxides: properties and mechanisms of formation. *Annu Rev Earth Planet Sci* 32:287–328
- Tebo BM, Johnson HA, McCarthy JK, Templeton AS (2005) Geomicrobiology of Manganese(II) oxidation. *Trends Microbiol* 13:421–428
- Lanson B, Drits VA, Silvester E, Manceau A (2000) Structure of H-exchange hexagonal birnessite and its mechanism of formation from Na-rich monoclinic buserite at low pH. *Am Miner* 85:826–838
- Manceau A, Drits VA, Silvester E, Bartoli C, Lanson B (1997) Structural mechanism of Co²⁺ oxidation by the phyllosulfate buserite. *Am Miner* 82:1150–1175
- Manceau A, Lanson M, Geoffroy N (2007) Natural speciation of Ni, Zn, Ba, and As in ferromanganese coatings on quartz using X-ray fluorescence, absorption, and diffraction. *Geochim Cosmochim Acta* 71:95–128
- Bargar JR, Fuller CC, Marcus MA, Brearley AJ, Perez De la Rosa M, Webb SM, Caldwell WA (2009) Structural characterization of terrestrial microbial Mn oxides from Pinal Creek, AZ. *Geochim Cosmochim Acta* 73:889–910
- Hochella MF Jr, Kasama T, Putnis A, Putnis CV, Moore JN (2005) Environmentally important, poorly crystalline Fe/Mn hydrous oxides: Ferrihydrite and a possibly new vernadite-like mineral from the Clark Fork River Superfund Complex. *Am Miner* 90:718–724
- Peña J, Bargar JR, Sposito G (2015) Copper sorption by the edge surfaces of synthetic birnessite nanoparticles. *Chem Geol* 396:196–207
- Simanova AA, Kwon KD, Bone SE, Bargar JR, Refson K, Sposito G, Peña J (2015) Probing the sorption reactivity of the edge surfaces in birnessite nanoparticles using Nickel(II). *Geochim Cosmochim Acta* 164:191–204
- Aplin AC, Cronan DS (1985) Ferromanganese oxide deposits from the Central Pacific Ocean, I. Encrustations from the Line Islands Archipelago. *Geochim Cosmochim Acta* 49:427–436
- Chukhrov FV, Sakharov BA, Gorshkov AI, Drits VA, Dikov YP (1985) Crystal structure of birnessite from the Pacific ocean. *Int Geol Rev* 27:1082–1088
- Duff MC, Hunter DB, Triay IR, Bertsch PM, Reed DT, Sutton SR, Shea-McCarthy G, Kitten J, Eng P, Chipera SJ, Vaniman DT (1999) Mineral associations and average oxidation states of sorbed Pu on Tuff. *Environ Sci Technol* 33:2163–2169
- Exon NF, Raven MD, De Carlo EH (2002) Ferromanganese nodules and crusts from the Christmas Island Region, Indian Ocean. *Mar Georesour Geotechnol* 20:275–297
- Friedl G, Wehrli B, Manceau A (1997) Solid phases in the cycling of manganese in eutrophic lakes: new insights from EXAFS spectroscopy. *Geochim Cosmochim Acta* 61:275–290
- Isaure M-P, Manceau A, Geoffroy N, Laboudigue A, Tamura N, Marcus MA (2005) Zinc mobility and speciation in soil covered by contaminated dredged sediment using micrometer-scale and bulk-averaging X-ray fluorescence, absorption and diffraction techniques. *Geochim Cosmochim Acta* 69:1173–1198
- Koschinsky A, Halbach P (1995) Sequential leaching of marine ferromanganese precipitates: Genetic implications. *Geochim Cosmochim Acta* 59:5113–5132
- Koschinsky A, Hein JR (2003) Uptake of elements from seawater by ferromanganese crusts: solid-phase associations and seawater speciation. *Mar Geol* 198:331–351
- Lienemann C-P, Tallefert M, Perret D, Gaillard J-F (1997) Association of cobalt and manganese in aquatic systems: chemical and microscopic evidence. *Geochim Cosmochim Acta* 61:1437–1446
- Manceau A, Lanson B, Schlegel ML, Harge JC, Musso M, Eybert-Berard L, Hazemann J-L, Chateigner D, Lambie GM (2000) Quantitative Zn speciation in smelter-contaminated soils by EXAFS spectroscopy. *Am J Sci* 300:289–343
- Manceau A, Tamura N, Celestre RS, MacDowell AA, Geoffroy N, Sposito G, Padmore HA (2003) Molecular-scale speciation of Zn and Ni in soil ferromanganese nodules from loess soils of the Mississippi Basin. *Environ Sci Technol* 37:75–80
- Manceau A, Tommaseo C, Rihs S, Geoffroy N, Chateigner D, Schlegel M, Tisserand D, Marcus MA, Tamura N, Chen Z-S (2005) Natural speciation of Mn, Ni, and Zn at the micrometer scale in a clayey paddy soil using X-ray fluorescence, absorption, and diffraction. *Geochim Cosmochim Acta* 69:4007–4034
- Marcus MA, Manceau A, Kersten M (2004) Mn, Fe, Zn and As speciation in a fast-growing ferromanganese marine nodule. *Geochim Cosmochim Acta* 68:3125–3136
- McKenzie RM (1980) The adsorption of lead and other heavy metals on oxides of manganese and iron. *Aust J Soil Res* 18:61–73
- Ostwald J, Frazer FW (1973) Chemical and mineralogical investigations on deep sea manganese nodules from the Southern Ocean. *Miner Deposita* 8:303–311
- Peacock CL, Moon EM (2012) Oxidative scavenging of thallium by birnessite: explanation for thallium enrichment and stable isotope fractionation in marine ferromanganese precipitates. *Geochim Cosmochim Acta* 84:297–313
- Peacock CL, Sherman DM (2007) Crystal-chemistry of Ni in marine ferromanganese crusts and nodules. *Am Miner* 92:1087–1092
- Takahashi Y, Manceau A, Geoffroy N, Marcus MA, Usui A (2007) Chemical and structural control of the partitioning of Co, Ce, and Pb in marine ferromanganese oxides. *Geochim Cosmochim Acta* 71:984–1008
- Peña J, Bargar JR, Sposito G (2011) Role of bacterial biomass in the sorption of Ni by biomass-birnessite assemblages. *Environ Sci Technol* 45:7338–7344
- Peña J, Kwon KD, Refson K, Bargar JR, Sposito G (2010) Mechanisms of nickel sorption by a bacteriogenic birnessite. *Geochim Cosmochim Acta* 74:3076–3089
- Lafferty BJ, Ginder-Vogel M, Sparks DL (2011) Arsenite oxidation by a poorly-crystalline manganese oxide. 3. Arsenic and manganese desorption. *Environ Sci Technol* 45:9218–9223
- Lafferty BJ, Ginder-Vogel M, Zhu M, Livi KJT, Sparks DL (2010) Arsenite oxidation by a poorly crystalline manganese-oxide. 2. Results from X-ray absorption spectroscopy and X-ray diffraction. *Environ Sci Technol* 44:8467–8472
- Manning BA, Fendorf SE, Bostick B, Suarez DL (2002) Arsenic(III) oxidation and arsenic(V) adsorption reactions on synthetic birnessite. *Environ Sci Technol* 36:976–981
- Tournassat C, Charlet L, Bosbach D, Manceau A (2002) Arsenic(III) oxidation by birnessite and precipitation of Manganese(II) arsenate. *Environ Sci Technol* 36:493–500
- Ying SC, Kocar BD, Fendorf S (2012) Oxidation and competitive retention of arsenic between iron- and manganese oxides. *Geochim Cosmochim Acta* 96:294–303
- Bidoglio G, Gibson PN, O'Gorman M, Roberts KJ (1993) X-ray absorption spectroscopy investigation of surface redox transformations of thallium

- and chromium on colloidal mineral oxides. *Geochim Cosmochim Acta* 57:2389–2394
45. Grangeon S, Manceau A, Guilhermet J, Gaillot A-C, Lanson M, Lanson B (2012) Zn sorption modifies dynamically the layer and interlayer structure of vernadite. *Geochim Cosmochim Acta* 85:302–313
 46. Bodei S, Manceau A, Geoffroy N, Baronnet A, Buatier M (2007) Formation of todorokite from vernadite in Ni-rich hemipelagic sediments. *Geochim Cosmochim Acta* 71:5698–5716
 47. Chukhrov FV (1980) Structural varieties of todorokite. *Int Geol Rev* 22:75–83
 48. Ostwald J (1984) Two varieties of lithiophorite in some Australian deposits. *Miner Mag* 48:383–388
 49. Grangeon S, Lanson B, Lanson M (2014) Solid-state transformation of nanocrystalline phyllosilicate into tectomanganate: influence of initial layer and interlayer structure. *Acta Crystallogr Sect B Struct Sci Cryst Eng Mater* 70:828–838
 50. Portehault D, Cassaignon S, Baudrin E, Jolivet J-P (2009) Structural and morphological control of manganese oxide nanoparticles upon soft aqueous precipitation through $\text{MnO}_4^-/\text{Mn}^{2+}$ reaction. *J Mater Chem* 19:2407–2416
 51. Cui H, Feng X, Tan W, He J, Hu R, Liu F (2009) Synthesis of todorokite-type manganese oxide from Cu-buserite by controlling the pH at atmospheric pressure. *Microporous Mesoporous Mater* 117:41–47
 52. Cui H, Liu X, Tan W, Feng X, Liu F, Ruan HD (2008) Influence of Mn(III) availability on the phase transformation from layered buserite to tunnel-structured todorokite. *Clays Clay Miner* 56:397–403
 53. Feng XH, Zhu MQ, Ginder-Vogel M, Ni CY, Parikh SJ, Sparks DL (2010) Formation of nano-crystalline todorokite from biogenic Mn oxides. *Geochim Cosmochim Acta* 74:3232–3245
 54. Zhang Q, Xiao Z, Feng X, Tan W, Qiu G, Liu F (2011) α - MnO_2 nanowires transformed from precursor δ - MnO_2 by refluxing under ambient pressure: the key role of pH and growth mechanism. *Mater Chem Phys* 125:678–685
 55. Manceau A, Lanson M, Takahashi Y (2014) Mineralogy and crystal chemistry of Mn, Fe Co, Ni, and Cu in a deep-sea Pacific polymetallic nodule. *Am Miner* 99:2068–2083
 56. Aplin AC, Cronan DS (1985) Ferromanganese oxide deposits from the Central Pacific Ocean, II. Nodules and associated sediments. *Geochim Cosmochim Acta* 49:437–451
 57. Dutta RK, Sideras-Haddad E, Connell SH (2001) Distribution of various components in a hydrogenous ferromanganese nodule and an Afanasiy Nikitin Seamount crust from Indian Ocean: a geochemical study using micro-PIXE. *Nucl Instrum Methods Phys Res Sect B* 181:545–550
 58. Węgorzewski AV, Kuhn T (2014) The influence of suboxic diagenesis on the formation of manganese nodules in the Clarion Clipperton nodule belt of the Pacific Ocean. *Mar Geol* 357:123–138
 59. Golden DC, Chen CC, Dixon JB (1986) Synthesis of Todorokite. *Science* 231:717–719
 60. Atkins AL, Shaw S, Peacock CL (2014) Nucleation and growth of todorokite from birnessite: implications for trace-metal cycling in marine sediments. *Geochim Cosmochim Acta* 144:109–125
 61. Baeyens B, Bradbury MH (1997) A mechanistic description of Ni and Zn sorption on Na-montmorillonite. 1. Titration and sorption measurements. *J Contam Hydrol* 27:199–222
 62. Bradbury MH, Baeyens B (1997) A mechanistic description of Ni and Zn sorption on Na-montmorillonite. 2. Modelling. *J Contam Hydrol* 27:223–248
 63. Tournassat C, Grangeon S, Leroy P, Giffaut E (2013) Modeling specific pH dependent sorption of divalent metals on montmorillonite surfaces. A review of pitfalls, recent achievements and current challenges. *Am J Sci* 313:395–451
 64. Silvester E, Manceau A, Drits VA (1997) Structure of synthetic monoclinic Na-rich birnessite and hexagonal birnessite; II, Results from chemical studies and EXAFS spectroscopy. *Am Miner* 82:962–978
 65. Buatier MD, Guillaume D, Wheat CG, Herve L, Adatte T (2004) Mineralogical characterization and genesis of hydrothermal Mn oxides from the flank of the Juan de Fuca Ridge. *Am Miner* 89:1807–1815
 66. Xu H, Chen T, Konishi H (2010) HRTEM investigation of trilling todorokite and nano-phase Mn-oxides in manganese dendrites. *Am Miner* 95:556–562
 67. Drits VA, Lanson B, Gaillot A-C (2007) Birnessite polytype systematics and identification by powder X-ray diffraction. *Am Miner* 92:771–788
 68. Giovanoli R (1980) Vernadite is random-stacked birnessite. *Miner Deposita* 15:251–253
 69. Grangeon S, Lanson B, Lanson M, Manceau A (2008) Crystal structure of Ni-sorbed synthetic vernadite: a powder X-ray diffraction study. *Miner Mag* 72:1197–1209
 70. Manceau A, Marcus MA, Grangeon S, Lanson M, Lanson B, Gaillot AC, Skanthakumar S, Soderholm L (2013) Short-range and long-range order of phyllosilicate nanoparticles determined using high-energy X-ray scattering. *J Appl Crystallogr* 46:193–209
 71. Zhu M, Ginder-Vogel M, Parikh SJ, Feng X-H, Sparks DL (2010) Cation effects on the layer structure of biogenic Mn-oxides. *Environ Sci Technol* 44:4465–4471
 72. Portehault D, Cassaignon S, Baudrin E, Jolivet J-P (2007) Morphology control of cryptomelane type MnO_2 nanowires by soft chemistry. Growth mechanisms in aqueous medium. *Chem Mater* 19:5410–5417
 73. Galindo HM, Carvajal Y, Njagi E, Ristau RA, Suib SL (2010) Facile one-step template-free synthesis of uniform hollow microstructures of cryptomelane-type manganese oxide K-OMS-2. *Langmuir* 26:13677–13683
 74. Usui A, Mita N (1995) Geochemistry and mineralogy of a modern buserite deposit from a hot spring in Hokkaido, Japan. *Clays Clay Miner* 43:116–127
 75. Post JE, Veblen DR (1990) Crystal structure determinations of synthetic sodium, magnesium, and potassium birnessite using TEM and the Rietveld method. *Am Miner* 75:477–489
 76. Fabian C, Reimann C, Fabian K, Birke M, Baritz R, Haslinger E (2014) GEMAS: Spatial distribution of the pH of European agricultural and grazing land soil. *Appl Geochem* 48:207–216
 77. Burns RG, Burns VM (1977) Mineralogy of manganese nodules. In: Glasby GP (ed) Marine manganese deposits. Elsevier, New York
 78. Burns RG, Burns VM (1979) Manganese oxides. In: Burns RG (ed) Marine minerals. Mineral Society of America, Washington, DC
 79. Feng XH, Tan WF, Liu F, Wang JB, Ruan HD (2004) Synthesis of todorokite at atmospheric pressure. *Chem Mater* 16:4330–4336
 80. Lee J, Ju JB, Cho WI, Cho BW, Oh SH (2013) Todorokite-type MnO_2 as a zinc-ion intercalating material. *Electrochim Acta* 112:138–143
 81. Marafatto FF, Strader ML, Gonzalez-Holguera J, Schwartzberg A, Gilbert B, Peña J (2015) Rate and mechanism of the photoreduction of birnessite (MnO_2) nanosheets. *Proc Natl Acad Sci* 112:4600–4605
 82. Plancon A (2002) CALCIPOW: a program for calculating the diffraction by disordered lamellar structures. *J Appl Crystallogr* 35:377
 83. Drits VA, Tchoubar C (1990) X-ray diffraction by disordered lamellar structures: theory and applications to microdivided silicates and carbons. Springer, Berlin
 84. Hadi J, Grangeon S, Warmont F, Seron A, Grenèche J-M (2014) A novel and easy chemical-clock synthesis of nanocrystalline iron-cobalt bearing layered double hydroxides. *J Colloid Interface Sci* 434:130–140
 85. Villalobos M, Lanson B, Manceau A, Toner B, Sposito G (2006) Structural model for the biogenic Mn oxide produced by *Pseudomonas putida*. *Am Miner* 91:489–502
 86. Grangeon S, Claret F, Lerouge C, Warmont F, Sato T, Anraku S, Numako C, Linard Y, Lanson B (2013) On the nature of structural disorder in calcium silicate hydrates with a calcium/silicon ratio similar to tobermorite. *Cem Concr Res* 52:31–37
 87. Grangeon S, Claret F, Linard Y, Chiaberge C (2013) X-ray diffraction: a powerful tool to probe and understand the structure of nanocrystalline calcium silicate hydrates. *Acta Crystallogr Sect B Struct Sci* 69:465–473
 88. Marty NCM, Grangeon S, Warmont F, Lerouge C (2015) Alteration of nanocrystalline calcium silicate hydrate (C–S–H) at pH 9.2 and room temperature: a combined mineralogical and chemical study. *Miner Mag* 79:437–458
 89. Gates WP, Slade PG, Manceau A, Lanson B (2002) Site occupancies by iron in nontronites. *Clays Clay Miner* 50:223–239
 90. Roosz C, Grangeon S, Blanc P, Montouillout V, Lothenbach B, Henocq P, Giffaut E, Vieillard P, Gaboreau S (2015) Crystal structure of magnesium silicate hydrates (M–S–H): The relation with 2:1 Mg–Si phyllosilicates. *Cem Concr Res* 73:228–237
 91. Vicat J, Fanchon E, Strobel P, Tran Qui D (1986) The structure of $\text{K}_{1.33}\text{Mn}_8\text{O}_{16}$ and cation ordering in hollandite-type structures. *Acta Crystallogr Sect B* 42:162–167

92. Hammersley A (1997) FIT2D: an introduction and overview. European Synchrotron Radiation Facility Internal Report ESRF97HA02T
93. Juhas P, Davis T, Farrow CL, Billinge SJL (2013) PDFgetX3: a rapid and highly automatable program for processing powder diffraction data into total scattering pair distribution functions. *J Appl Crystallogr* 46:560–566
94. Farrow C, Juhas P, Liu J, Bryndin D, Božin E, Bloch J, Proffen T, Billinge S (2007) PDFfit2 and PDFgui: computer programs for studying nanostructure in crystals. *J Phys Condens Matter* 19:335219

Publish with **ChemistryCentral** and every scientist can read your work free of charge

“Open access provides opportunities to our colleagues in other parts of the globe, by allowing anyone to view the content free of charge.”

W. Jeffery Hurst, The Hershey Company.

- available free of charge to the entire scientific community
- peer reviewed and published immediately upon acceptance
- cited in PubMed and archived on PubMed Central
- yours — you keep the copyright

Submit your manuscript here:
<http://www.chemistrycentral.com/manuscript/>



Chemistry Central

Electronic Annex

to the article:

“Cryptomelane formation from nanocrystalline vernadite precursor: a high energy X-ray scattering and transmission electron microscopy perspective on reaction mechanisms”

authored by Sylvain Grangeon, Alejandro Fernandez-Martinez, Fabienne Warmont, Alexandre Gloter, Nicolas Marty, Agnieszka Poulain & Bruno Lanson

Supplementary data 1: Anisotropic Debye-Waller factors (U), scale factor, correlated motion related quadratic term coefficient (Delta2) and particule size (Spdiameter) retrieved from analysis of PDF data.

Species (if applicable)	Parameter	Sample			
		MndBi3_10y	MndBi4_10y	MndBi8_10y	MndBi10_10y
Mn	U(11) and U(22) (Å ²)	0.003	0.001	0.002	0.001
	U(33) (Å ²)	0.006	0.01	0.013	0.022
Layer O and O from ⁵⁵ Mn coordination sphere	U(11) and U(22) (Å ²)	0.001	0.003	0.003	0.004
	U(33) (Å ²)	0.074	0.045	0.07	0.061
Na and interlayer H ₂ O	U(11), U(22) and U(33) (Å ²)	0.001	0.004	0.001	0.001
Scale factor		1.43	1.45	1.43	1.36
Delta2		2.85	2.53	3.17	2.93
Spdiameter (Å)		18.91	17.13	17.31	18.33

Note: Delta2 and U(33) from O suffer from uncertainties, as they were correlated.

Electronic Annex

to the article:

“Cryptomelane formation from nanocrystalline vernadite precursor: a high energy X-ray scattering and transmission electron microscopy perspective on reaction mechanisms”

authored by Sylvain Grangeon, Alejandro Fernandez-Martinez, Fabienne Warmont, Alexandre Gloter, Nicolas Marty, Agnieszka Poulain & Bruno Lanson

Supplementary data 2: Example of the sensitivity of calculated XRD patterns to the number of interlayer $^{\text{TC}}\text{Mn}^{3+}$. The experimental pattern from MndBi8_10y is the black solid line and the red solid line is the best simulation (in which the abundance of $^{\text{TC}}\text{Mn}^{3+}$ is 0.13 per layer octahedron). Solid green line: $^{\text{TC}}\text{Mn}^{3+}$ reduced to 0.08 per layer octahedron. Solid brown line: $^{\text{TC}}\text{Mn}^{3+}$ increased to 0.18 per layer octahedron. All other parameters remained identical in all simulations.

Only the [11, 20] band was calculated, as it is the most sensitive to the number of interlayer species sorbed in a TC configuration.

